Ordered arrays of II/VI diluted semiconductor quantum wires: formation within mesoporous MCM-41 silica

Alois Loidl, Felix J. Brieler, Michael Fröba, Limei Chen, Peter J. Klar, Wolfram Heimbrodt, Hans-Albrecht Krug von Nidda

Angaben zur Veröffentlichung / Publication details:

Loidl, Alois, Felix J. Brieler, Michael Fröba, Limei Chen, Peter J. Klar, Wolfram Heimbrodt, and Hans-Albrecht Krug von Nidda. 2002. "Ordered arrays of II/VI diluted semiconductor quantum wires: formation within mesoporous MCM-41 silica." Chemistry - A European Journal 8 (1): 185–94. https://doi.org/10.1002/1521-3765(20020104)8:1%3C185::AID-CHEM185%3E3.0.CO;2-L.

Ordered Arrays of II/VI Diluted Magnetic Semiconductor Quantum Wires: Formation within Mesoporous MCM-41 Silica

Felix J. Brieler,[a] Michael Fröba,*[a] Limei Chen,[b] Peter J. Klar,*[b] Wolfram Heimbrodt,[b] Hans-Albrecht Krug von Nidda,[c] and Alois Loidl[c]

Abstract: We present a novel way of synthesising highly ordered arrays of hollow $Cd_{1-x}Mn_xS$ quantum wires with lateral dimensions of 3 – 4 nm separated by 1 – 2 nm SiO_2 barriers by forming $Cd_{1-x}Mn_xS$ ($0 \leq x \leq 1$) semiconductors inside the pore system of mesoporous MCM-41 SiO_2 host structures. X-ray diffraction and transmission electron microscopy (TEM) studies reveal the hexagonal symmetry of these arrays (space group *p6m*) and confirm the high degree of order. Physisorption measurements show the filling of the pores of the MCM-41 SiO_2. The X-ray absorption near-edge structure (XANES), extended X-ray absorption fine structure (EXAFS), electron paramagentic resonance (EPR), and Raman studies confirm the good crystalline quality of the incorporated (Cd,Mn)S guest. The effects of reducing the lateral dimensions on the magnetic and electronic properties of the diluted magnetic semiconductor were studied by photoluminescence (PL) and PL excitation spectroscopy and by SQUID and EPR measurements in the temperature range 2 – 400 K. Due to the quantum confinement of the excitons in the wires, an increase of about 200 meV in the direct band gap was observed. In addition, the p-d hybridisation-related bowing of the band gap as a function of Mn concentration in the wires is much stronger than in the bulk. This effect is related to the increase in the band gap due to quantum confinement, which shifts the p-like valence band edge closer to the 3d-related states of Mn in the valence band. Thus, the p-d hybridisation and the strength of the band gap bowing are increased. Compared to bulk (II,Mn)VI compounds, antiferromagnetic coupling between the magnetic moments of the Mn^{2+} ions is weaker. For the samples with high Mn concentrations ($x > 0.8$) this leads to a suppression of the phase transition of the Mn system from paramagnetic to antiferromagnetic. This effect can be explained by the fact that the lateral dimensions of the wires are smaller than the magnetic length scale of the antiferromagnetic ordering.

[a] Prof. Dr. M. Fröba,[+] Dipl.-Chem. F. J. Brieler
Institute of Inorganic and Analytical Chemistry
Justus-Liebig-University Giessen
Heinrich-Buff-Ring 58, 35392 Giessen (Germany)
Fax: (+49)-641-99-34109
E-mail: michael.froeba@anorg.chemie.uni-giessen.de

[b] Dr. P. J. Klar, Dr. L. Chen, Prof. Dr. W. Heimbrodt
Department of Physics and Materials Science Centre
Philipps-University of Marburg
Renthof 5, 35032 Marburg (Germany)
Fax: (+49)-6421-28-27036
E-mail: Klarp@mailer.uni-marburg.de

[c] Dr. H.-A. Krug von Nidda, Prof. Dr. A. Loidl
Department of Physics
University of Augsburg
Augsburg (Germany)

[+] Former affiliations during the period of this research project:
Institute of Inorganic and Applied Chemistry, University of Hamburg, Hamburg (Germany)
Institute of Inorganic Chemistry, University of Erlangen-Nuremberg, Erlangen (Germany)

Introduction

The group of molecular sieves was enriched in 1992 by the discovery of a new family of materials called M41S phases.[1] These materials expanded the range of pore sizes from the micro- to the mesoporous range, and this attracted great attention for size-selective applications such as catalysis,[2–4] nanostructured host – guest compounds[5] and sorption materials.[6] The original synthetic pathway used tetraalkylammonium halides as structure-directing agents and tetraethyl orthosilicate (TEOS) as the silica source under alkaline conditions. This route led to three types of mesostructured materials: hexagonal (MCM-41), cubic (MCM-48) and lamellar (MCM-50). Since then a variety of syntheses has been developed. Different kinds of amphiphilic molecules have been utilised, for example, nonionic[7] or neutral surfactant molecules,[8] which lead not only to powders but also to thin films[9] and even monolithic structures.[10] The range of different morphologies enhances the options for possible

applications; for example, the catalytic properties of these materials can be extended by the incorporation of guest species such as Ti,[11, 12] Zr,[13] V,[14] Fe,[15, 16] Co,[17] Sn[18] and Pt[19] into the pore structure. Inclusion chemistry in the pore system has a wide field of possible chemical applications, such as sorption, ion exchange or polymerisation inside the channels.[5] The intrapore formation of catalytically active nanostructured compounds such as Fe_2O_3[20] or $CoFe_2O_4$[21] into the cubic, three-dimensional pore structure of MCM-48 makes this material suitable for catalytic applications, as well as providing compounds with new physical and structural properties.

The uniform, rod-like pore structure of MCM-41 provides other interesting possibilities. From a physical point of view, these mesoporous SiO_2 materials are ideal host materials for semiconductors due to their high degree of order and the large band gap of SiO_2, which serves as barrier material. Semiconductor compounds that have been implanted into MCM-41 SiO_2 to give regular arrays of quantum wires include CdS,[22] CdSe,[23] GaAs,[24] InP,[25] Ge[26] and SiGe.[27] In general, some of the optical properties of semiconductor nanostructures (e.g., exciton binding energies, oscillator strengths, nonlinearities) are enhanced relative to the bulk material due to the smaller dimensions.[28, 29]

Recently, we reported preliminary results on the first incorporation of the diluted magnetic semiconductor $Cd_{1-x}Mn_xS$ into MCM-41 SiO_2.[30] Diluted magnetic semiconductors (DMS) are formed when the cation A of a semiconductor AB is partially substituted by a magnetic ion M to give an $A_{1-x}M_xB$ structure. A large subgroup of the DMS are the (II,Mn)VI semiconductors in which a fraction x of the the Group II cations are substituted by Mn^{2+} ions.[31, 32] Due to its half-filled 3d shell with a spin of $S = 5/2$, manganese has a large magnetic moment, and the magnetic phase diagram of the ternary compound is accordingly rich. Besides a paramagnetic phase, a spin-glass phase and an antiferromagnetic phase are known. In the paramagnetic phase, the exchange interaction between the localised magnetic moments of the Mn^{2+} ions and the spins of the extended band states leads to so-called giant Zeeman splitting of the band states of up to about 100 meV at magnetic fields of only a few tesla. This s,p-d exchange interaction constitutes a unique interplay between semiconductor properties and magnetism.

Ordered arrays of identical magnetic clusters are of recent scientific and technological interest.[33–37] They may provide a way of studying the link between magnetism on a microscopic atomic level and the macroscopic magnetic state. Interesting properties are expected as the geometrical dimensions of the clusters become comparable to the characteristic nanoscopic and mesoscopic length scales (e.g., magnetic exchange length, domain width).[33, 34] Ordered arrays of nanomagnets are also promising components for new devices in magneto- or spin electronics (e.g., magnetic hard-disc media, nonvolatile computer memory chips).[38] Most previous work on ordered arrays of magnetic clusters focussed on metal clusters. For achieving a high degree of order, the fabrication of the arrays usually involves a pattern-definition process. Various techniques are in use, for example, electron-beam lithography, X-ray lithography and pattern definition assisted by scanning tunnelling microscopy.[34]

Far less work has been carried out on magnetic semiconductor nanostructures.[39–45] For metal structures, a high degree of order could only be obtained so far by combining lithographic pattern definition with epitaxial semiconductor-growth techniques, either by growing structures on patterned substrates[42] or by post-growth patterning and etching of the epitaxial semiconductor layers.[45] However, the smallest lateral sizes achievable by these techniques are much larger than 10 nm. Other approaches, such as DMS clusters in silicate glass,[39, 40] DMS clusters in reverse micelles[41] and self-assembly by Stranski–Krastanov growth[43] yield cluster sizes below 10 nm but give a much smaller degree of order.

The synthesis of DMS nanostructures is of great interest, as they combine semiconducting and magnetic properties in the same nanostructure. Here, we give a detailed account of the synthesis of $Cd_{1-x}Mn_xS$ nanoparticles ($x = 1-100\,\%$) in a highly ordered MCM-41 silica matrix and discuss the effect of the reduced dimensions on the magnetic and electronic properties of the DMS.

Results and Discussion

Powder X-ray diffraction: From the powder X-ray diffraction pattern of the pristine calcined MCM-41 silica, the hexagonal symmetry of the space group $p6m$ can clearly be indexed (Figure 1). A high degree of long-range order and a relatively thin wall thickness (ca. 1–2 nm) can be assumed on the basis of the reflections at higher angles 2θ. After the intrapore formation of the DMS compound (in this case $Cd_{0.9}Mn_{0.1}S$) the peaks in the X-ray powder diffraction (XRD) are reduced in intensity and slightly shifted to smaller d spacings.

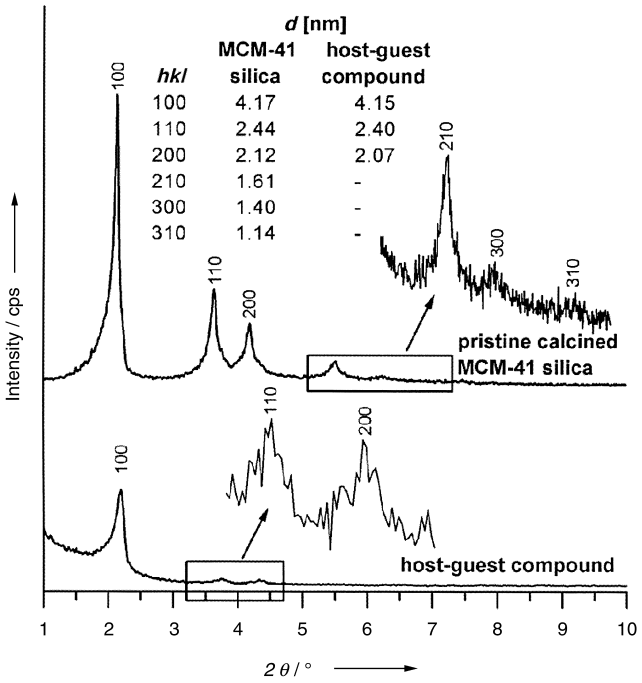

Figure 1. Powder X-ray diffraction patterns of pristine calcined MCM-41 silica and an MCM-41 $SiO_2/Cd_{0.9}Mn_{0.1}S$ host–guest compound.

The loss in intensity is due to the fact that the introduction of scattering material into the pores leads to an increased phase cancellation between scattering from the walls and the pore regions. Therefore, the intensities of the Bragg reflections are lower. This very sensitive phase relationship was first described as a theoretical model[46] and was recently substantiated by experimental data.[20, 21, 47]

The contraction of mesoporous structures on calcination or thermal treatment in acidic solutions is due to the influence of the impregnation treatment, which is accompanied by thermal treatment. It probably increases the connectivity within the silica walls and results in a small contraction of the structure.[20, 21, 48] In the region between $2\theta = 20^\circ$ and 60° no reflections of the bulk DMS compounds are present. The observed features are the same for all incorporated samples $Cd_{1-x}Mn_xS$.

Physisorption measurements: Figure 2 shows the amount of physisorbed nitrogen (at 77 K) versus the relative pressure p/p_0 for pristine calcined MCM-41 silica and a representative sample. Both isotherms are of type IV, typical for a mesoporous material.[49] The step that indicates capillary condensation within the pores is at $p/p_0 = 0.3-0.4$. The amount of adsorbed nitrogen strongly decreases after the incorporation of the semiconductor, as does the specific inner surface area.

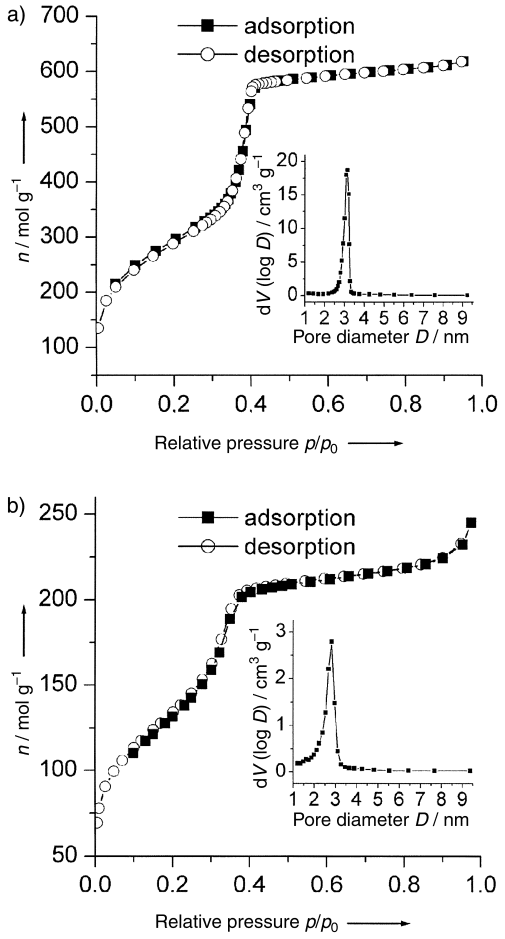

Figure 2. Nitrogen adsorption/desorption isotherms at 77 K of the pristine calcined MCM-41 silica (a) and an MCM-41 $SiO_2/Cd_{0.95}Mn_{0.05}S$ host–guest compound (b).

The position of the step evoked by capillary condensation is shifted to lower relative pressure due to the decrease in pore size. After the incorporation of the semiconductor the specific BET surface of the mesoporous compound is reduced by more than 60% (for $x = 0.2$) with respect to MCM-41 silica. The calculated BET surface area and the mean pore diameter for all samples are listed in Table 1. Note that the introduction of the heavy elements cadmium and manganese itself leads to a decrease in the specific surface area of the MCM-41 silica matrix.[6, 20] The mean pore diameter was calculated by using the model of Barrett, Joyner and Halenda,[50] although this well-established theory is actually valid for materials with pores larger than 4 nm and underestimates the diameter of mesopores by approximately 1 nm.[51, 52] However, it is an appropriate method for determining changes in the pore-size distribution.[6] After the intrapore formation of the different semiconductor compounds, mesoporosity can still be found. The lack of change in the type of the isotherm proves the conservation of the cylindrical pore system. However, a decrease in the mean pore diameter is indicated by the shift of the main peak of the pore-size distribution to smaller values and additional broadening due to a shoulder at smaller pore sizes. In addition, the wall thickness increases (see Table 1). These results clearly indicate coating of the walls of the pores (hollow wires) and even partial filling.

Table 1. BET surface area, mean pore diameter D and wall thickness w (calculated from $w = a - D$; a = lattice constant) for the pristine MCM-41 silica material and the MCM-41 silica/semiconductor host–guest compounds.

Sample	BET surface area [$m^2 g^{-1}$]	Mean pore diameter D [nm]	Wall thickness w [nm]
Pristine MCM-41 SiO_2	1108	3.2	1.6
MCM-41 $SiO_2/Cd_{0.95}Mn_{0.05}S$	478	2.8	2.0
MCM-41 $SiO_2/Cd_{0.9}Mn_{0.1}S$	501	2.8	2.0
MCM-41 $SiO_2/Cd_{0.85}Mn_{0.15}S$	491	2.8	2.0
MCM-41 $SiO_2/Cd_{0.8}Mn_{0.2}S$	297	2.7	2.0
MCM-41 $SiO_2/Cd_{0.5}Mn_{0.5}S$	156	3.2	2.2
MCM-41 $SiO_2/Cd_{0.1}Mn_{0.9}S$	410	2.8	2.0
MCM-41 SiO_2/CdS	383	2.8	2.1
MCM-41 SiO_2/MnS	574	2.8	2.0

Transmission electron microscopy: Figure 3 shows transmission electron micrographs of representative regions of pristine calcined MCM-41 silica and an MCM-41/$Cd_{0.5}Mn_{0.5}S$ host–guest compound. The hexagonal arrangement of the pores can clearly be observed over a long range. Even after the impregnation/conversion cycle the pronounced long-range order is still intact. Furthermore no particles lying on the outer surface of the MCM-41 silica material can be detected, even on a larger length scale (Figure 3b). This supports the conclusion from powder X-ray diffraction and the nitrogen physisorption data that formation of the semimagnetic semiconductor nanoparticles took place predominantly inside the pore structure.

Infrared and Raman spectroscopy: To confirm that the conversion of the acetates to the sulfides by thermal treatment

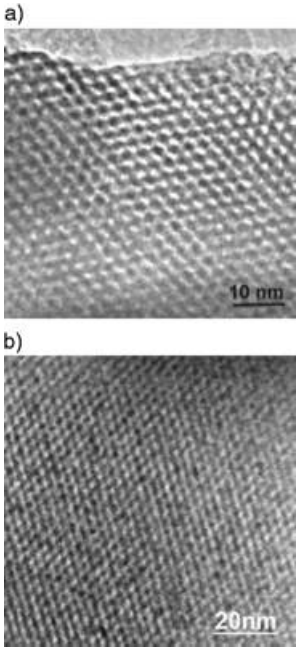

Figure 3. Transmission electron micrographs of the pristine calcined MCM-41 silica (a) and an MCM-41 $SiO_2/Cd_{0.5}Mn_{0.5}S$ host – guest compound (b).

in an H_2S atmosphere is a quantitative process, IR spectra of products were recorded after the various preparation steps during the impregnation/conversion cycle. The spectra of the MCM-41 silica/cadmium acetate host – guest compound is almost a sum of those of MCM-41 silica and bulk cadmium acetate (Figure 4). After the thermal treatment all bands

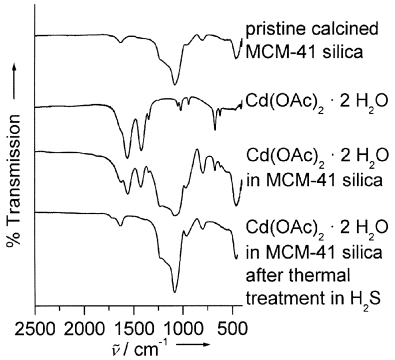

Figure 4. IR spectra taken during the impregnation/conversion cycle of an MCM-41 SiO_2/CdS host – guest compound.

corresponding to the acetate have vanished, and the IR spectrum of the finished product is similar to that of calcined MCM-41 silica. As (Cd,Mn)S has no phonon modes above 400 cm^{-1}, this suggests quantitative conversion of the acetate to the sulfide within the pore structure. This is further confirmed by the Raman spectra in Figure 5. The room-temperature Raman spectra of the MCM-41 $SiO_2/Cd_{1-x}Mn_xS$ host – guest compounds clearly show features corresponding to the longitudinal optical (LO) mode and 2LO phonon modes of $Cd_{1-x}Mn_xS$ at about 300 and 600 cm^{-1}, respectively. The slight shift of the LO phonon mode to higher wavenumber and the development of a shoulder for $x > 10\,\%$ are in

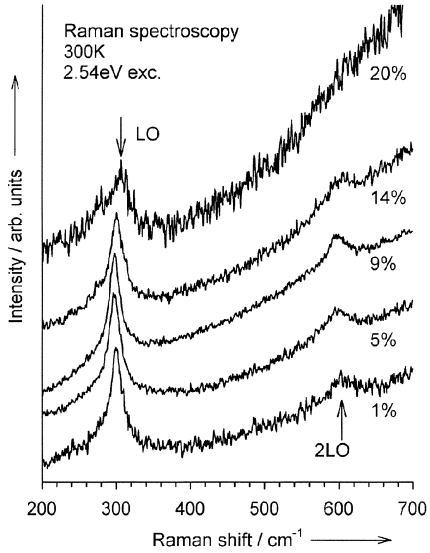

Figure 5. Raman spectra of different MCM-41 $SiO_2/Cd_{1-x}Mn_xS$ host – guest compounds with $x \leq 20\,\%$.

good agreement with the results for corresponding bulk crystalline samples.[53, 54] The increasing noise level with increasing x is due to a strong luminescent background.

X-ray absorption spectroscopy: X-ray absorption spectroscopy addresses the question whether the guest species in the MCM-41 silica pore structure are segregated cadmium sulfide and manganese sulfide or whether the Mn^{2+} ions are incorporated into the cadmium sulfide matrix. Figure 6 shows

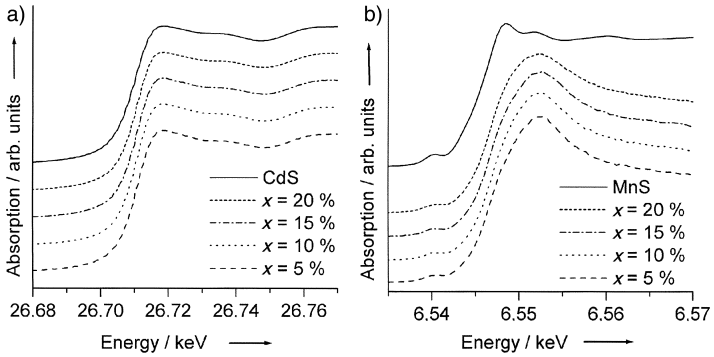

Figure 6. Normalised Cd K-XANES (a) and Mn K-XANES (b) spectra of the host – guest compounds with $x \leq 20\,\%$ and the bulk reference samples.

the normalized X-ray absorption near-edge structure (XANES) regions of the Cd K-edge (Figure 6a) and Mn K-edge spectra (Figure 6b), which can be used as "fingerprints" of the respective materials. All spectra recorded at the Cd K-edge look very similar, and the resemblance of spectra of the host – guest compounds to the CdS reference spectrum indicates formation of cadmium sulfide in the pores. Furthermore, the spectra of the host – guest compounds recorded at the Mn K-edge show no similarity to that of the bulk reference material MnS. The features in the XANES region of the spectrum of the reference material cannot be found in those of the host – guest compounds. This is a first indication that no

MnS was formed in the pores, yet manganese is present in the samples.

Further proof for the formation of DMS nanoparticles in the pores of MCM-41 material is provided by the modified radial distribution functions (not phase-corrected) extracted from the extended X-ray absorption fine structure (EXAFS) oscillations shown in Figure 7. In the Cd K-EXAFS spectra

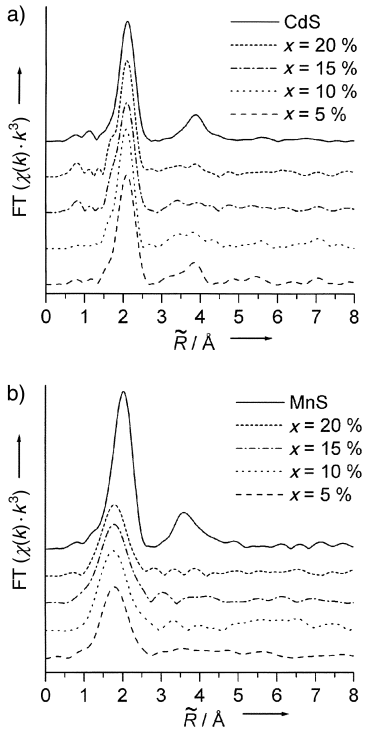

Figure 7. Modified radial distribution functions (not phase-corrected) of the Cd K-EXAFS (a) and Mn K-EXAFS (b) spectra of the host – guest compounds with $x \leq 20\,\%$ and the bulk reference sampless.

(Figure 7a) the first CdS shell at 2.52 Å can be observed for the CdS reference and all MCM-41 silica/$Cd_{1-x}Mn_xS$ host – guest compounds. The next-nearest neighbour shell (CdCd) is only observed in the reference and the sample with the lowest Mn content. This is proof of the distortion of the CdS matrix due to a lager amount of distributed manganese. Table 2 lists the fit results of the Cd K-edge measurements. In the Mn K-EXAFS spectra the corresponding next-nearest neighbour shell (MnCd) can be recognised in the reference material (wurtzite structure) but not in any of the host – guest compounds. The first MnS shell of the host – guest compounds

Table 2. Fit results of the Cd K-EXAFS measurements. Abbreviations: N = coordination number, R = bond length, $\Delta\sigma^2$ = Debye – Waller factor, ΔE = energy shift.

Sample	N	R [Å]	$\Delta\sigma^2$ [10^{-3} Å^2]	ΔE_0
CdS (reference)[a]	4/12	2.52/4.12	3.9/1.5	2.69/1.84
MCM-41 $SiO_2/Cd_{0.95}Mn_{0.05}S$	4.81	2.52	5.4	3.10
MCM-41 $SiO_2/Cd_{0.9}Mn_{0.1}S$	4.29	2.51	4.5	1.93
MCM-41 $SiO_2/Cd_{0.85}Mn_{0.15}S$	4.47	2.52	5.2	2.99
MCM-41 $SiO_2/Cd_{0.8}Mn_{0.2}S$	4.36	2.52	5.0	3.20

[a] The amplitude reduction factor $S_0^2 = 1.0254$ was obtained from the reference compound by keeping the coordination numbers constant.

is clearly shifted to smaller distances. In addition, it shows a reduced coordination number. Both effects are caused by a local disorder in the CdS matrix arising from the substitution of Cd by Mn to give a distorted MnS geometry. Hence, it can be concluded that Mn^{2+} ions replace Cd^{2+} ions in the nanocrystalline structure, and a $Cd_{1-x}Mn_xS$ nanocrystal is formed. Table 3 gives an overview of the fit results of the Mn K-EXAFS measurements.

Table 3. Fit results of the Mn K-EXAFS measurements. Abbreviations: N = coordination number, R = bond length, $\Delta\sigma^2$ = Debye – Waller factor, ΔE = energy shift.

Sample	N	R [Å]	$\Delta\sigma^2$ [10^{-3}Å^2]	ΔE_0
MnS (wurtzite)[a]	4.01	2.44	4.5	2.53
MCM-41 $SiO_2/Cd_{0.95}Mn_{0.05}S$	3.41	2.37	9.9	– 6.81
MCM-41 $SiO_2/Cd_{0.9}Mn_{0.1}S$	3.28	2.37	10.1	– 6.76
MCM-41 $SiO_2/Cd_{0.85}Mn_{0.15}S$	3.67	2.33	11.1	– 10.45
MCM-41 $SiO_2/Cd_{0.8}Mn_{0.2}S$	3.02	2.36	10.1	– 6.98

[a] The amplitude reduction factor $S_0^2 = 0.7795$ was obtained from MnS with manganese in octahedral coordination geometry (rock salt structure).

Photoluminescence spectroscopy: Figure 8 shows a schematic diagram of the complex optical processes observable in wide-gap (II,Mn)VI semiconductors. The semiconductor band states with a direct band-gap transition and the 3d shells of

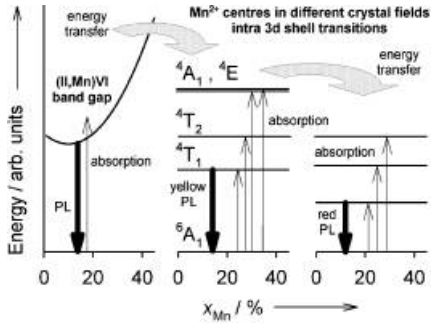

Figure 8. Schematic diagram of the optical processes observable in wide-gap (II,Mn)VI semiconductors. The abscissa values are the same for all three graphs.

the Mn^{2+} ions with their internal transitions form subsystems of the (II,Mn)VI semiconductor which are coupled by energy-transfer processes. In addition to semiconductor band-gap-related luminescence and absorption, luminescence and absorption bands due to the intra-3d-shell transitions of the Mn^{2+} ions are observed. The states within the 3d shell are strongly affected by the crystal field of the lattice site of the corresponding Mn^{2+} ion. The majority of the Mn^{2+} ions are incorporated on cation sites with a tetrahedral crystal field. The lowest state is the $^6A_1$ state originating from the ^6S state of the free ion, and the next higher states are $^4T_1$, $^4T_2$, $^4A_1$ and ^4E originating from the ^4G state of the free ion. Absorption processes can take place between the $^6A_1$ ground state and the excited states. A yellow luminescence between the $^4T_1$ first excited state and the $^6A_1$ ground state is observed for all wide-gap (II,Mn)VI compounds, independent of Mn concentration. In addition, there are a few Mn^{2+} ions on other sites. These

"defect" sites show a different crystal-field splitting between the states of the 3d shell, and this leads to other absorption and luminescence bands. A prominent example is the red Mn^{2+} luminescence. Energy-transfer processes can take place between the band states and the Mn^{2+} 3d shells, as well as between Mn^{2+} 3d shells corresponding to different sites.

Figure 9 depicts photoluminescence (PL) spectra recorded at 10 K of five MCM-41 silica/$Cd_{1-x}Mn_xS$ samples ($x = 1$–20 %) recorded at low excitation densities. The PL spectra for $x \geq 5$ % are very similar and consist of two overlapping

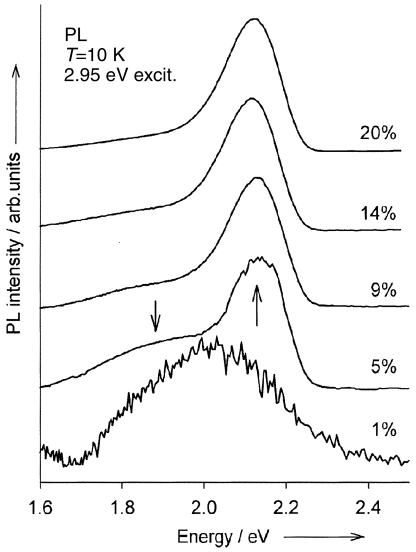

Figure 9. Low-temperature Mn-related photoluminescence bands of MCM-41 silica/$Cd_{1-x}Mn_xS$ with $x \leq 20$ %.

broad bands: a dominant yellow band centered at 2.1 eV and a red band at about 1.8 eV (marked by arrows). The yellow PL band originates from the 3d internal transition of Mn^{2+} on a Cd site. The transition takes place between the $^4T_1$ first excited state and the $^6A_1$ ground state. The red PL band originates from the 3d internal transition of another Mn^{2+}-related defect, which either also has tetrahedral site symmetry but a different crystal field or corresponds to a site with octahedral symmetry. The two bands can be excited individually at higher excitation densities (i.e., laser excitation).[55] For excitation energies above 2.4 eV, the PL is dominated by the yellow luminescence band. Laser excitation at energies below the yellow PL band excites only the red PL band.[55] These PL bands are typical for (Cd,Mn) and (Zn,Mn) mixed chalcogenide crystals.[32, 56, 57] Because of the efficient energy transfer from the $Cd_{1-x}Mn_xS$ band states into the Mn^{2+} subsystem, there is no band-gap-related excitonic PL in the continuous-wave measurement. The PL of the sample with $x = 1$ % is very weak and probably consists of an additional deep defect band in addition to the two Mn-related bands.

Temperature-dependent PL spectra of the Mn emission of MCM-41 silica/$Cd_{0.95}Mn_{0.05}S$ are shown as a typical example in Figure 10. The peak positions of the two emission bands hardly shift in energy with increasing temperature, and both bands broaden. These are typical features of the Mn 3d internal transitions. However, the spectra in Figures 9 and 10

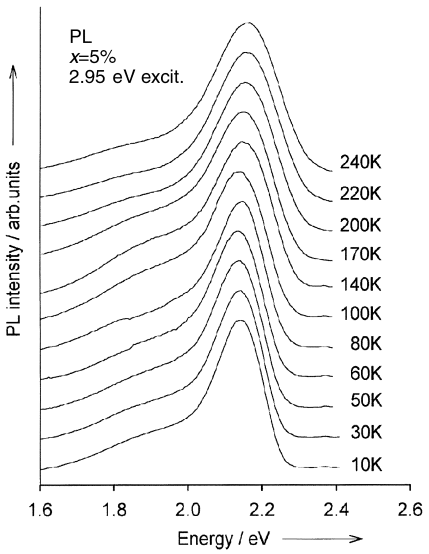

Figure 10. Temperature dependence of the Mn-related photoluminescence bands of an MCM-41 $SiO_2/Cd_{0.95}Mn_{0.05}S$ host–guest compound.

differ from those of bulk (Cd,Mn)S crystals in that the red Mn emission band does not increase in intensity relative to the yellow band, neither with increasing temperature nor with increasing Mn concentration x. The unusual concentration dependence can be taken as an indication of the good crystalline quality of the incorporated (Cd,Mn)S nanoparticles, as the red emission is usually assigned to Mn^{2+} on sites other than the cation sites of the wurtzite lattice. The unusual temperature dependence might indicate that the transfer processes from the band states and the yellow-emitting Mn centres into the red-emitting Mn centres are altered by the reduction of the dimensionality from three in the bulk material to one or quasizero in the nanoparticles. However, this needs to be studied in greater detail.

Photoluminescence excitation (PLE) spectroscopy: The PLE spectra recorded at 10 K (Figure 11) are in good agreement with the discussion of the PL data in Figures 9 and 10. The difference between the PLE spectra detected on the yellow emission (thick lines) and those detected on the red emission (thin lines) confirms the assignment of the PL bands to the two Mn centres. The PLE spectra corresponding to the yellow band show a distinct peak which varies significantly with x. For the MCM-41 silica/$Cd_{0.99}Mn_{0.01}S$ sample the peak is at about 2.95 eV, it has its lowest energy for $x = 5$ % sample at 2.75 eV, and increases gradually to about 2.85 eV for $x = 9$, 14, and 20 %. This concentration dependence clearly shows that these signals correspond to the band gap of the incorporated (Cd,Mn)S compound, as peaks corresponding to absorption of the 3d shell of Mn^{2+} would not depend on x.[32] This shows that the yellow emission arises predominantly from an energy transfer from the band states to yellow-emitting centres. The PLE spectra of the red PL of the samples with $x = 5$–20 % are very similar. They do not exhibit a signal related to the (Cd,Mn)S band gap, but a broad peak centred at about 2.4 eV corresponding to the absorption $^6A_1 \rightarrow {}^4T_1$ of yellow-emitting Mn^{2+} centres, which is Stokes-shifted by about 200 meV relative to the yellow emission due to strong electron–

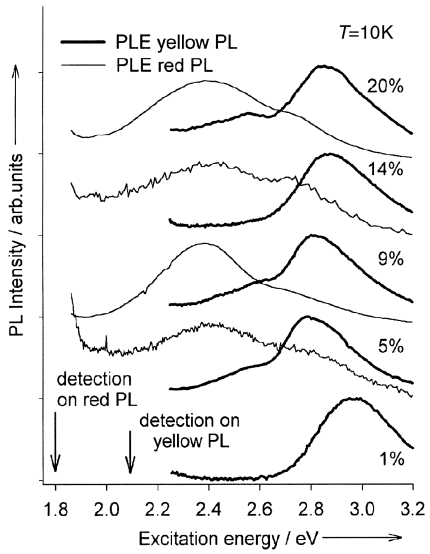

Figure 11. Photoluminescence excitation spectra of the host–guest compounds with $x \leq 20\,\%$, detected for the yellow luminescence (thick lines) and the red luminescence (thin lines).

phonon coupling in the (II,Mn)VI materials. The small band-gap-related feature and the existence of an absorption peak corresponding to the yellow-emitting centre in the PLE spectrum of the red-emitting centre show that, as in bulk (II,Mn)VI compounds, the red emission is mainly a result of an energy transfer from the yellow-emitting centres to the red centres.

Figure 12 compares the band-gap energies obtained from the PLE spectra of the yellow PL band with those of bulk $Cd_{1-x}Mn_xS$.[58] The solid lines are guides to the eye and represent the bowing of the the pd exchange-induced band

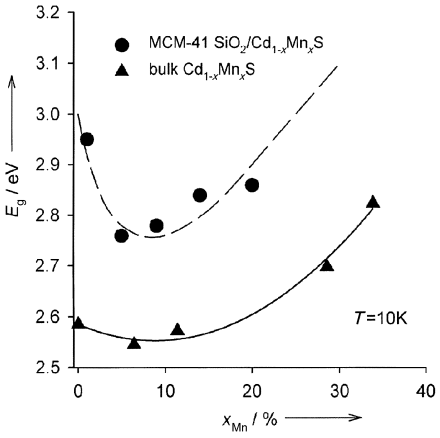

Figure 12. Dependence of the direct band gap on Mn concentration for MCM-41 silica/$Cd_{1-x}Mn_xS$ host–guest compounds and $Cd_{1-x}Mn_xS$ bulk crystals at 10 K. The lines are guides to the eye.

gap.[59] The band-gap data of the $Cd_{1-x}Mn_xS$ quantum wires show that the quantum confinement energy in the wires is greater than 200 meV, which confirms the presence of an intrapore nanostructured semiconductor. Similar confinement energies were observed for $Cd_{1-x}Mn_xS$ nanoparticles of comparable size that were synthesised in reverse micelles.[41] An increase in the p-d exchange-induced band-gap bowing is observed for the quantum wires, and this is also in good agreement with previous studies.[41] A possible explanation for this effect is an enhancement of the p-d exchange interaction caused by modified positions of the p- and d-related bands in the band structure of the quantum wires compared to the bulk. Due to the quantum confinement, the lowest valence-band state of the $Cd_{1-x}Mn_xS$ quantum wires is shifted significantly towards the Mn 3d states, which are positioned about 3 eV below the valence-band edge of the bulk material. This enhancement effect is similar to that in bulk $Cd_{1-x}Mn_xY$ (Y = Te, Se, S), for which increased p-d hybridisation is observed with increasing band gap on going from Te to S.[60]

Electron paramagnetic resonance (EPR) spectroscopy: Figure 13 shows EPR spectra of seven MCM-41 silica/$Cd_{1-x}Mn_xS$ powder samples with $x = 1$, 5, 9, 14, 20, 90 and 100 %. For $45 < x < 80\,\%$ there is a miscibility gap for $Cd_{1-x}Mn_xS$. The

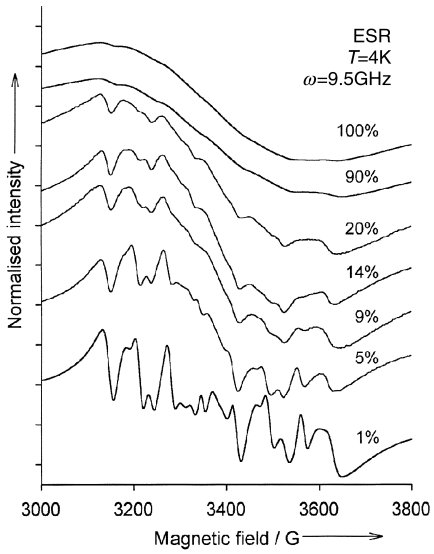

Figure 13. Normalised EPR spectra of seven host–guest compound powder samples of different Mn contents x at $T = 4$ K.

two miscibility regions may have different crystal structures: wurtzite for the low-x region and rock salt or wurtzite for the high-x region. All spectra were recorded at 4 K and normalised to the same amplitude. In reality, their relative intensities roughly increase with increasing Mn concentration. However, we observed deviations from simple proportionality, which can be ascribed to different degrees of implantation for the seven samples. The EPR spectra are typical for exchange-coupled Mn^{2+} ions in (Cd,Mn) and (Zn,Mn) mixed chalcogenide crystals.[61–63] The features in the EPR spectra can be best explained for low x. The spectra consist of a sextet of sharp lines, each of which has a pair of satellites at lower magnetic field on a broad background. The g-factor is 2.001. The sharp lines and their satellites correspond to the allowed ($\Delta m_S = \pm 1$, $\Delta m_I = 0$) and forbidden ($\Delta m_S = \pm 1$, $\Delta m_I = \pm 1$) hyperfine transitions of the Zeeman-split $m_S = -1/2$ and $m_S = +1/2$ levels of the $^6S_{5/2}$ (or $^6A_1$) ground state of the Mn^{2+} 3d

electrons. The hyperfine structure arises from the interaction between the $S = 5/2$ spin of the unpaired 3d electrons with the $I = 5/2$ spin of the Mn^{2+} nucleus. The $\Delta m_S = \pm 1$ transition energies between the Zeeman levels $m_S = \pm 5/2$ and $m_S = \pm 3/2$, as well as $m_S = \pm 3/2$ and $m_S = \pm 1/2$, vary with changing crystal orientation in the range of about 20 G with respect to the $m_S = -1/2$ to $m_S = +1/2$ transitions.[61] Therefore, the corresponding sextets of lines cannot be distinguished in the spectrum of powder samples, but their average determines the width of the six resonance lines. The prominent forbidden hyperfine transitions in the spectra are typical for Mn^{2+} ions in the tetrahedral environment of a Cd site in a wurtzite crystal. In a zinc blende crystal these should be much weaker.[61, 64] Thus, the crystal structure of all five $Cd_{1-x}Mn_xS$ wires of the low-x miscibility region is wurtzite. Note that that CdS nanoclusters with low manganese contents often have the zinc blende structure.[64] We also reported a zinc blende structure for $Cd_{0.985}Mn_{0.015}S$ in MCM-41 silica.[55] For $Cd_{1-x}Mn_xS$ nanoparticles with an x value of a few percent, zinc blende and wurtzite structures seem to have very similar total energies, so that both crystal structures might occur, depending on the preparation process and the size of the nanoparticles. This is also suggested by calculations on the bulk material and clusters.[65, 66] With increasing x the structures in the EPR spectra are broadened and even disappear for $x = 90$ and 100%, and the broad background strongly increases due to increasing superexchange interaction between the Mn^{2+} ions.[67, 68] Therefore, no information about the crystal structure in the high-x miscibility region can be obtained from EPR spectra.

As in bulk (II,Mn)VI materials, the integral EPR signal corresponding to the Mn^{2+} absorption has a Lorentzian line shape in the paramagnetic regime.[67] Overall intensity I_{total} and line width ΔH of the Lorentzian are very sensitive to the spin–spin correlations of the Mn^{2+} ions. Therefore, changes in the magnetic order with temperature, for example, transitions from the paramagnetic to the spin-glass phase or antiferromagnetic phase, are reflected in the temperature dependence of ΔH and I_{total}.[67, 68] The main graph of Figure 14 depicts plots of ΔH versus temperature for various MCM-41 silica/$Cd_{1-x}Mn_xS$ powder samples. Temperature trends and magnitudes of ΔH for the samples with $x \leq 20\%$ are similar to those reported for the bulk material.[67] However, the increase in ΔH with decreasing temperature appears to be weaker than for bulk crystals, and this suggests that the spin ordering leading to the spin-glass phase is suppressed in the nanocrystals. The suppression of the spin–spin correlations due to the nanostructuring becomes more pronounced for samples with high x, on the other side of the miscibility gap. $Cd_{1-x}Mn_xS$ bulk crystals with $x > 80\%$ show a phase transition from paramagnetic to antiferromagnetic with a Néel temperature of $T_N = 152$ K for MnS and 127 K for $Cd_{0.1}Mn_{0.9}S$ for the rock salt modification and $T_N = 80$ K for the wurtzite modification of MnS. This is reflected in the EPR spectrum by a singularity in the EPR line width ΔH on approaching T_N from higher temperatures and a vanishing EPR signal below T_N.[68] Powder samples with micrometer grains and thin films evaporated onto glass substrates show similar anomalies, but not as distinct, at a T_N that is about 20 K lower. In contrast, the

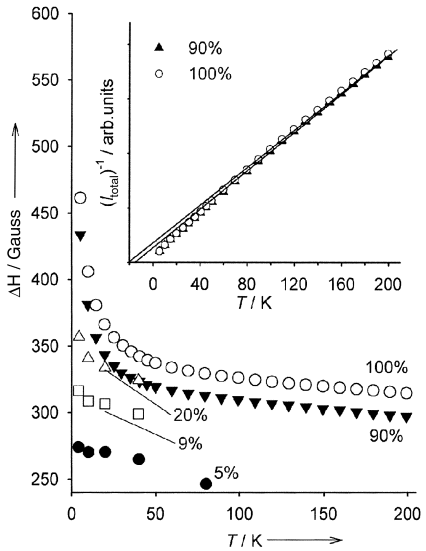

Figure 14. Temperature dependence of the line width of the EPR absorption signal for various host–guest compounds. Inset: Plot of reciprocal intensity of the EPR absorption signal versus temperature for MCM-41 silica/$Cd_{0.1}Mn_{0.9}S$ and MCM-41 silica/MnS.

MCM-41 silica/$Cd_{0.1}Mn_{0.9}S$ and MCM-41 silica/MnS powder samples show an increasing ΔH and an increasing intensity down to the lowest temperature in the experiment, that is, the Néel temperature of the two samples must be lower than 4 K. The Curie–Weiss parameter Θ of the paramagnetic phase can be obtained by linear extrapolation of a plot of the reciprocal EPR intensity I_{total}^{-1} versus temperature T (Figure 14, inset). The intersection of the straight lines with the T axis below 0 K confirms the antiferromagnetic coupling between the Mn^{2+} spins. For both samples it yields a value of $\Theta \approx 20$ K. However, this value of Θ is about 20 times lower than that of bulk MnS.[32]

The results of the SQUID measurements in Figure 15 fully confirm the EPR results. Plotting the reciprocal dc magnetic susceptibility χ^{-1} of the MCM silica/$Cd_{1-x}Mn_xS$ samples as a function of temperature basically yields straight lines. Hence,

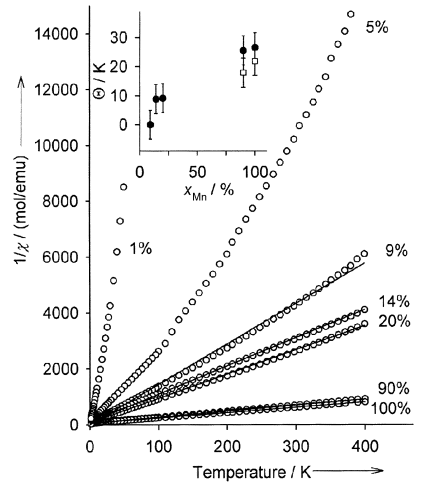

Figure 15. Temperature dependence of the reciprocal magnetic susceptibility for various MCM-41 silica/$Cd_{1-x}Mn_xS$. Inset: Plot of the Curie–Weiss parameter as a function of Mn content obtained by SQUID (●) and EPR (□) on these samples.

no transition from the paramagnetic to the spin-glass phase for $x \leq 20\,\%$ or to the antiferromagnetic phase for $x > 80\,\%$ takes place in the temperature range from 400 down to 1.8 K. The deviations from linear behaviour, in particular for $x < 10\,\%$ and above 200 K, are mainly due to experimental difficulties as the magnitude of the susceptibility χ approaches the detection limit. Fitting the plots for $x \geq 9\,\%$ by using the dependence $\chi^{-1}(T) \sim (T + \Theta)$ for the paramagnetic region allows one to determine the Curie–Weiss parameter Θ as a function of x (Figure 15, inset). The Θ values obtained by analysing the SQUID data agree well with those obtained by EPR spectroscopy. As expected, Θ increases with increasing Mn content. The results of the EPR and the SQUID measurements lead to the conclusion that the antiferromagnetism in the MCM-41 silica/$Cd_{1-x}Mn_xS$ samples is strongly suppressed due to the reduced dimensions of the nanowires.

Conclusion

The results of the various applied techniques confirm that high-quality nanostructured $Cd_{1-x}Mn_xS$ ($x = 1-100\,\%$) was formed and stabilised in the pore system of MCM-41 silica matrices. Optical and EPR spectroscopic measurements show the strong effect of the reduced dimensions on the electronic and magnetic properties of $Cd_{1-x}Mn_xS$. Besides the well-known quantum confinement effect, which leads to an increase in the direct band gap in nanoclusters by more than 200 meV compared to the bulk, an increase of the p-d exchange-induced band-gap bowing as a function of x was observed. This effect is probably due to the modified positions of the p- and d-related bands in the band structure of the $Cd_{1-x}Mn_xS$ wires. In addition, spin–spin correlations between the $S = 5/2$ spins of the Mn^{2+} ions, which lead to the transition from the paramagnetic phase to the spin-glass phase for $20 < x < 45\,\%$ and to the transition from the paramagnetic phase to the antiferromagnetic phase for $x > 80\,\%$ in bulk $Cd_{1-x}Mn_xS$, are strongly suppressed in the nanostructures. This becomes clear in the temperature-dependent EPR and SQUID studies on MCM-41 silica/$Cd_{1-x}Mn_xS$, in which no phase transitions were observed down to 2 K for all x, and Curie–Weiss parameters Θ in the paramagnetic regime that are more than an order of magnitude smaller than in bulk $Cd_{1-x}Mn_xS$ reflect the strong reduction of the antiferromagnetic coupling between Mn^{2+} spins.

Experimental Section

Synthesis of mesoporous MCM-41 silica: Hexadecyl trimethylammonium bromide (C_{16}TABr, 0.25 mol, Merck) was dissolved in water (35 mol) by stirring and heating to 65 °C. Tetramethylammonium hydroxide (TMAOH, 0.2 mol, 25 % in water, Merck) and, with vigorous stirring, SiO_2 (1 mol, Cab-O-Sil, Riedel-de-Haen) were added. The mixture was stirred at 65 °C for 30 min, transferred into a Teflon-lined steel autoclave and stored at room temperature for 24 h. The autoclave was then statically heated to 150 °C for 24 h. The resultant white precipitate was collected by filtration and washed several times with warm deionised water. Drying at room temperature under vacuum gave a white powder, which was calcined in flowing air at 550 °C for 6 (heating rate: 1 K min^{-1}).

Synthesis of the MCM-41 silica/DMS host–guest materials: Impregnation was carried out by stirring calcined MCM-41 silica (0.5 g) in a 0.5 M solution of cadmium acetate (Merck) and manganese acetate (Merck) with the desired Cd/Mn ratio for 10 min. No further adjustment of the pH value was carried out. The dispersion was separated by centrifugation. The residue was dried in vacuum and stored in an H_2S atmosphere at 70 °C for 48 h. Elemental analyses revealed a very good agreement of the Cd/Mn ratio in the host–guest compound with the initial Cd/Mn ratio. The content of the SiO_2 matrix with metal ions was 40–50 wt %. For detailed information on the respective samples, see Table 1.

Analyses and measurements: Powder X-ray diffraction patterns were recorded at room temperature on a Bruker AXS D8 Advance diffractometer ($Cu_{K\alpha}$) in θ/θ geometry with a secondary monochromator.

Physisorption measurements were carried out with a Quantachrome Autosorb 1 instrument with nitrogen as adsorptive at 77 K. Before each sorption measurement the sample was outgassed at 100 °C for at least 24 h under turbomolecular pump vacuum.

Infrared spectra were recorded on a Perkin-Elmer FT-IR 1720 in the range 400–4000 cm^{-1} in shuttle mode. Phonon Raman spectra were obtained at room temperature by using a Raman microscope system. An argon ion laser operating at 488 nm was used for excitation, and a Jobin-Yvon T64000 triple Raman spectrometer in subtractive mode with a CCD detector for detection.

The transmission electron micrographs were recorded on a Philips CM 300 UT and on a Philips CM 30 ST. The XAFS measurements on the K-edges of Cd and Mn were recorded at HASYLAB at DESY on the beamlines X-1.1 for Cd and E-4 for Mn. All data were recorded at room temperature with a silicon (111) monochromator for the Mn K-edge (fluorescence mode) and a silicon (311) monochromator for the Cd K-edge absorption spectra (transmission mode). For data analyses the programs FEFF WinXAS[69] and 7.01[70] were used.

The photoluminescence-based optical measurements were carried out in the temperature range 10–300 K. Tuneable monochromatic excitation light with a band width of 5 nm was provided by a tungsten lamp followed by a 0.25 m monochromator. The sample luminescence was detected with a 0.5 m spectrometer equipped with a GaAs photomultiplier with a resolution better than 1 nm. For the PL measurements the sample was excited with 420 nm light (2.95 eV), and the PL signal detected in the range 450–900 nm. For the photoluminescence excitation (PLE) measurements, the PL intensity was detected at 580 nm or at 700 nm by varying the wavelength of the excitation light from 350 to 560 nm and 350 to 680 nm, respectively.

Electron paramagnetic resonance measurements on a Bruker Elexsys 500 CW spectrometer at X-band frequencies (9.48 GHz) and magnetic fields up to 1 T were performed between 4 and 200 K in a continuous-flow He cryostat.

The dc susceptibility of the samples was measured in the temperature range from 1.8 to 400 K by using a Quantum Design SQUID magnetometer operating at 1 kOe.

Acknowledgements

The authors thank Dr. Kathrin Hofmann (Institute of Inorganic and Analytical Chemistry, Justus-Liebig University Giessen) and Andreas Kornowski (Institute of Physical Chemistry, University of Hamburg) for the transmission electron micrographs, Dr. Thorsten Ressler (Fritz-Haber-Intitut, MPG Berlin) for recording the Mn K-edge X-ray absorption fluorescence spectra and Dana Vieweg (Dept. Physics, University of Augsburg) for carrying out the SQUID measurements. We are grateful to Dr. Matthias Schreck (Dept. Physics, University of Augsburg) for giving us the opportunity of using his Raman equipment. Financial support by the Deutsche Forschungsgemeinschaft (Fr 1372/4-1, 4-2 and He 2298/4-1, 4-2) and the Fonds der Chemischen Industrie is gratefully acknowledged.

[1] C. T. Kresge, M. E. Leonowicz, W. J. Roth, J. C. Vartulli, J. S. Beck, *Nature* **1992**, *359*, 710.
[2] A. Corma, *Chem. Rev.* **1997**, *97*, 2373.

[3] U. Ciesla, F. Schüth, *Microporous Mesoporous Mater.* **1999**, *27*, 131.
[4] a) J. Y. Ying, C. P. Mehnert, M. S. Wong, *Angew. Chem.* **1999**, *38*, 58; b) J. Y. Ying, C. P. Mehnert, M. S. Wong, *Angew. Chem. Int. Ed.* **1999**, *38*, 56.
[5] K. Möller, T. Bein, *Chem. Mater.* **1998**, *10*, 2950.
[6] M. Thommes, R. Köhn, M. Fröba, *J. Phys. Chem. B* **2000**, *104*, 7932.
[7] S. A. Bagshaw, E. Prouzet, T. J. Pinnavaia, *Science* **1995**, *269*, 1242.
[8] P. T. Tanev, T. J. Pinnavaia, *Science* **1995**, *267*, 865.
[9] D. Grosso, A. R. Balkenende, P. A. Albouy, M. Lavergne, L. Mazerolles, F. Babonneau, *J. Mater. Chem.* **2000**, *9*, 2085.
[10] N. A. Melosh, P. Lipic, F. S. Bates, F. Wudl, G. D. Stucky G. H. Fredrickson, B. F. Chmelka, *Macromolecules* **1999**, *32*, 4332.
[11] P. T. Tanev, M. Chibwe, T. J. Pinnavaia, *Nature* **1994**, *368*, 321.
[12] W. Zhang, M. Fröba, J. Wang, P. T. Tanev, J. Wong, T. J. Pinnavaia, *J. Am. Chem. Soc.* **1996**, *118*, 9164.
[13] M. Morey, G. D. Stucky, S. Schwarz, M. Fröba, *J. Phys. Chem. B* **1999**, *103*, 2037.
[14] K. M. Reddy, I. Moudrkovski, A. Sayari, *J. Chem. Soc. Chem. Commun.* **1994**, 1059.
[15] Z. Y. Tuan, S. Q. Liu, T. H. Chen, J. Z. Wang, H. X. Li, *J. Chem. Soc. Chem. Commun.* **1995**, 973.
[16] T. Abe, Y. Tachibana, T. Uematsu, M. Iwamoto, *J. Chem. Soc. Chem. Commun.* **1995**, 1617.
[17] A. Jentys, N. H. Pham, H. Vinek, M. Englisch, J. A. Lercher, *Microporous Mater.* **1996**, *6*, 13.
[18] T. K. Das, K. Chaudhari, A. J. Chandwadkar, S. Sivasanker, *Chem. Commun.* **1995**, 2495.
[19] U. Junges, W. Jacobs, I. Voigt-Martin, B. Krutzsch, F. Schüth, *Chem. Commun.* **1995**, 2283.
[20] M. Fröba, R. Köhn, G. Bouffaud, *Chem. Mater.* **1999**, *11*, 2858.
[21] R. Köhn, F. Brieler, M. Fröba, *Stud. Surf. Catal.* **2000**, *129*, 341.
[22] T. Hirai, H. Okubo, I. Komasawa, *J. Phys. Chem. B* **1999**, *103*, 4228.
[23] H. Parala, H. Winkler, M. Kolbe, A. Wohlfahrt, R. A. Fischer, R. Schmechel, H. von Seggern, *Adv. Mater.* **2000**, *12*, 1050.
[24] V. I. Srdanov, I. Alxneit, G. D. Stucky, C. M. Reaves, S. P. DenBaars, *J. Phys. Chem. B* **1998**, *102*, 3341.
[25] J. R. Agger, M. W. Anderson, M. E. Pemble, O. Terasaki, Y. Nozue, *J. Phys. Chem. B* **1998**, *102*, 3345.
[26] R. Leon, D. Margolese, G. Stucky, P. M. Petroff, *Phys. Rev. B* **1995**, *52*, R2285.
[27] Y. S. Tang, S. Cai, G. Jin, J. Duan, K. L. Wang, H. M. Soyez, B. S. Dunn, *Appl. Phys. Lett.* **1997**, *71*, 2449.
[28] R. N. Bhargava, *J. Lumin.* **1996**, *70*, 85.
[29] A. D. Yoffe, *Adv. Phys.* **1993**, *42*, 173.
[30] L. Chen, P. J. Klar, W. Heimbrodt, F. Brieler, M. Fröba, *Appl. Phys. Lett.* **2000**, *76*, 3531.
[31] J. K. Furdyna, *J. Appl. Phys.* **1988**, *64*, R29.
[32] O. Goede, W. Heimbrodt, *Phys. Stat. Sol. (B)* **1988**, *146*, 11.
[33] J. Shi, S. Gider, K. Babcock, D. D. Awschalom, *Science* **1996**, *271*, 937.
[34] M. Hehn, K. Ounadjela, J.-P. Bucher, F. Rousseaux, D. Decanini, B. Bartenlian, C. Chappert, *Science* **1996**, *272*, 1782.
[35] R. P. Cowburn, D. K. Koltsov, A. O. Adeyeye, M. E. Welland, *Appl. Phys. Lett.* **1998**, *73*, 3947.
[36] G. Meier, M. Kleiber, D. Grundler, D. Heitmann, R. Wiesendanger, *Appl. Phys. Lett.* **1998**, *72*, 2168.
[37] A. Maeda, M. Kume, T. Ogura, K. Kuroki, T. Yamada, M. Nishikawa, Y. Harada, *J. Appl. Phys.* **1994**, *76*, 6667.
[38] G. A. Prinz, *Science* **1998**, *282*, 1660.
[39] K. Yanata, K. Suzuki, Y. Oka, *J. Appl. Phys.* **1993**, *73*, 4595.
[40] Y. Wang, N. Herron, K. Möller, T. Bein, *Solid State Commun.* **1991**, *77*, 33.
[41] L. Levy, N. Feltin, D. Ingert, M. P. Pileni, *J. Phys. Chem. B* **1997**, *101*, 9153.
[42] L. Parthier, S. Luther, O. Portugall, M. von Ortenberg, K. Uchida, H. Kunimatsu, N. Miura, *J. Cryst. Growth* **1998**, *184/185*, 339.
[43] P. A. Crowell, V. Nikitin, J. A. Gupta, D. D. Awschalom, F. Flack, N. Samarth, *Physica E* **1998**, *2*, 854.
[44] S. A. Crooker, D. A. Tulchinsky, J. Levy, D. D. Awschalom, R. Garcia, N. Samarth, *Phys. Rev. Lett.* **1995**, *75*, 505.
[45] P. J. Klar, D. Wolverson, J. J. Davies, W. Heimbrodt, M. Happ, T. Henning, *Phys. Rev. B* **1998**, *57*, 7114.
[46] W. Hammond, E. Prouzet, S. D. Mahanti, T. J. Pinnavaia, *Microporous Mesoporous Mater.* **1999**, *27*, 19.
[47] R. Köhn, M. Fröba, *Catal. Today* **2001**, *68*, 227.
[48] M. Janicke, D. Kumar, G. D. Stucky, B. F. Chmelka in *Zeolites and Related Microporous Materials: State of the Art* (Eds.: J. Weitkamp, H. G. Karge, H. Pfeifer, W. Hölderich), Elsevier, Amsterdam, **1994**, p. 243.
[49] K. S. W. Sing, D. H. Everett, R. A. W. Haul, L. Moscou, R. A. Pierotti, J. Rouquérol, T. Siemieniewaska, *Pure Appl. Chem.* **1985**, *57*, 603.
[50] E. P. Barrett, L. G. Joyner, P. P. Halenda, *J. Am. Chem. Soc.* **1951**, *73*, 373.
[51] C. Lastokie, K. E. Gubbins, N. J. Quirke, *J. Phys. Chem. B* **1993**, *97*, 4786.
[52] P. I. Ravikovitch, S. C. O. Domhnaill, A. Neimark, F. Schüth, K. K. Unger, *Langmuir* **1995**, *11*, 4765.
[53] E.-K. Suh, A. K. Arora, A. K. Ramdas, S. Rodriguez, *Phys. Rev. B* **1992**, *45*, 3360.
[54] C. T. Tsai, S. H. Chen, D. S. Chuu, *Phys. Rev. B* **1996**, *54*, 11555.
[55] L. Chen, P. J. Klar, W. Heimbrodt, F. Brieler, M. Fröba, H.-A. Krug von Nidda, A. Loidl, *Physica E* **2001**, *10*, 369.
[56] O. Goede, W. Heimbrodt, V. Weinhold, *Phys. Stat. Sol. (B)* **1986**, *136*, K49.
[57] W. Heimbrodt, C. Benecke, O. Goede, H.-E. Gumlich, *Phys. Stat. Sol. (B)* **1989**, *154*, 405.
[58] C. T. Tsai, S. H. Chen, D. S. Chuu, W. C. Chou, *Phys. Rev. B* **1996**, *54*, 11555.
[59] R. B. Bylsma, W. M. Becker, J. Kossut, U. Debska, *Phys. Rev. B* **1986**, *33*, 8207.
[60] M. Taniguchi, M. Fujimori, M. Fujisawa, T. Mori, I. Souma, Y. Oka, *Solid State Commun.* **1987**, *62*, 431.
[61] J. Schneider, S. R. Sircar, A. Räuber, *Z. Naturforsch.* **1963**, *18a*, 980.
[62] J. Lambe, C. Kikuchi, *Phys. Rev.* **1960**, *119*, 1256.
[63] Y. Ishikawa, *J. Phys. Soc. Jpn* **1966**, *21*, 1473.
[64] D. M. Hofmann, A. Hofstaetter, U. Leib, B. K. Meyer, C. Counio, *J. Cryst. Growth* **1998**, *184/185*, 383.
[65] C.-Y. Yeh, Z. W. Lu, S. Froyen, A. Zunger, *Phys. Rev. B* **1992**, *45*, 12130.
[66] J.-O. Joswig, M. Springborg, G. Seifert, *J. Phys. Chem. B* **2000**, *104*, 2617.
[67] N. Samarth, J. K. Furdyna, *Phys. Rev. B* **1988**, *37*, 9227.
[68] O. Goede, D. Backs, W. Heimbrodt, M. Kanis, *Phys. Stat. Sol. B* **1989** *151*, 311.
[69] T. Ressler, *J. Synchrotron Rad.* **1998**, *5*, 118.
[70] J. J. Rehr, J. Mustre de Leon, S. I. Zabinsky, R. C. Albers *J. Am. Chem. Soc.* **1991**, *113*, 5135.